Investigation of 18-channel CWDM arrayed waveguide grating with silica-based waveguide

Wan-Chun Kim
Young-Sic Kim
Su-Yong Kim
Yoo-Chul Noh
Yang-Ki Song
Sung-Hyun Kang
Jin-Gu Pyo
Jin-Bong Kim

Investigation of 18-channel CWDM arrayed waveguide grating with silica-based waveguide

Wan-Chun Kim,[a,b,][*] Young-Sic Kim,[a,b] Su-Yong Kim,[a,b] Yoo-Chul Noh,[b] Yang-Ki Song,[b] Sung-Hyun Kang,[a,b] Jin-Gu Pyo,[b] and Jin-Bong Kim[b,c]
[a]Chonnam National University, Interdisciplinary Program for Photonic Engineering, 300 Yong-bong dong, Buk-gu, Gwangju 500-757, Republic of Korea
[b]PPI Inc., 958-10 Dae-chon dong, Buk-gu, Gwangju 500-470, Republic of Korea
[c]Chonnam National University, Department of Applied Chemical Engineering, 300 Yong-bong dong, Buk-gu, Gwangju 500-757, Republic of Korea

Abstract. Arrayed waveguide gratings (AWGs) are commonly used as multiplexers/demultiplexers in wavelength division multiplexing systems. We design and fabricate a coarse wavelength division multiplexing AWG with a wide free-spectral range. A gull-wing-shaped AWG layout and S-shaped AWG layout are used to understand a wide band range. The spectral difference between each layout is experimentally demonstrated. Our results indicate that the fabricated AWG is suitable for applications such as portable power meters. © *The Authors. Published by SPIE under a Creative Commons Attribution 3.0 Unported License. Distribution or reproduction of this work in whole or in part requires full attribution of the original publication, including its DOI.* [DOI: 10.1117/1.OE.55.8.087110]

1 Introduction

In recent years, arrayed waveguide gratings (AWGs) have become increasingly popular as wavelength multiplexers and demultiplexers for dense wavelength division multiplexing (DWDM) applications, such as long-haul networks and metropolitan networks.[1,2] On the other hand, cascaded optical thin film filters have occupied the largest market share in coarse wavelength division multiplexing (CWDM) applications because of their cheaper hardware cost and optical performance. In general, CWDM transmission is realized with 18 20-nm-spaced channels with wavelengths ranging between 1270 and 1610 nm. This setup allows optical fiber infrastructure to carry more data via the use of multiple wavelengths, thereby ensuring optical network reliability. This technology has been widely deployed for several classes of optical fiber communications, such as metropolitan and regional networks.[2] However, in subsidiary applications, such as portable optical power meters or spectrometers,[3–5] AWGs can serve as sufficiently small wavelength dividers in a CWDM grid. Although AWGs have certain advantages in terms of their small footprint and mass productivity, they have never been applied to wideband CWDMs because of their limitations with regard to design. On the other hand, from the perspective of AWG fabrication, silica waveguide (WG) technology is one of the most successfully commercialized technologies for AWGs because current silica fabrication processes offer quality WGs for passive optical devices. Thus, there is a need to further explore AWG application to CWDM.

In this study, we design, fabricate, and evaluate an 18-channel CWDM AWG with 20-nm channel spacing using the silica-on-silicon WG process with two previously publicized chip layouts.

2 Design of Coarse Wavelength Division Multiplexing Arrayed Waveguide Grating

The conventional straight-arc-straight geometry proposed by Dragone[6] cannot be used to fabricate a wide free-spectral range (FSR) AWG because of its minimum arrayed WG separation gap and the small optical path difference of each arrayed WG. Undesirable coupling between adjacent arrayed WGs causes optical phase distortion.[7] Accordingly, wide-FSR AWGs have been realized with the use of gull wing (GW)-shaped AWG layouts[8] and S-shaped AWG layouts,[9] with geometric calculations as reported by Ismail et al.[10]

In this paper, we report on an 18-channel CWDM AWG covering the wavelength range from 1250 to 1610 nm.

2.1 Arrayed Waveguide Grating Parameters

A silica-on-silicon WG with 1.0 delta% refractive index contrast was chosen for our study. The AWG design parameters are listed in Table 1.

The refractive indices of the core and cladding were calculated by means of the Sellmeier equation for fused silica[11] at 1440 nm. The effective indices of the channel and slab WG were calculated using the conventional effective index method.

2.2 Arrayed Waveguide Grating Input/Output Spectral Shape

To engineer a flat spectral response, a number of two-dimensional beam propagation simulations were performed for the input and output regions with the C2V Olympios software.[12]

A two-step exponentially tapered input and linearly tapered output were used. The fixed design parameters are listed in Table 2.

The appropriate spectral shape was obtained from iterative simulations: input, output, and in-out coupled field distributions, as shown in Figs. 1 and 2.

---

*Address all correspondence to: Wan-Chun Kim, E-mail: audckf@gmail.com

Table 1 Parameters for 20-nm-spaced 18-channel AWG.

Parameter	Value
Core size (μm)	4.5×6.0 (width $\times$ height)
Central wavelength (nm) Slab effective index	1440 1.45881
Core effective index	1.46137
Cladding effective index	1.44821
Diffraction order	3
Wavelength spacing (nm)	20
Channel spacing of arrayed WGs (μm)	9
Channel spacing of output WGs (μm)	27
Focal length (μm)	5811.58
Number of arrayed WGs	108
FSR (nm)	~472
Minimum bending radius of arrayed WGs (μm)	4500

2.3 Arrayed Waveguide Grating Layout

GW-shaped layout and S-shaped layout geometries were used in order to understand wide-band FSR AWGs. The schematic views of each layout are shown in Fig. 3.

For both the GW-shaped and S-shaped layouts, each WG in section I and section I′ consists of a straight WG ($S1$), an arc WG ($A1$), and a second straight WG ($S2$). In case of the S-shaped layout, the twisted section I′ is attached after the section III. The arrayed WGs in section I (section I′) have a constant path difference (section I: $\Delta L1 = \Delta S1 + \Delta A1 + \Delta S2$, section I′: $\Delta L3 = \Delta S2 + \Delta A1 + \Delta S1$, $\Delta L1 = \Delta L3$), and the endpoint of each WG in section I has the same separation (S) from the first to the last WG. Section II consists of an arc WG ($A2$) having constant path difference ($\Delta L2 = \Delta A2$). The total path difference is ($\Delta L1 + \Delta L2 + \Delta L3 = \Delta L$), and section II accommodates the excessive path differences from $\Delta L1 + \Delta L3$ ($\Delta L2$ is a negative value). Parameter $A2$ has a fixed radius decrement S and the same arc open angle. Parameter $\Delta L2$ is determined by its open angle and S.

In the case of the S-shaped layout, the construction of section I is the same as that of the GW-shaped layout, but the twisted section I′ is attached after section III. Therefore, the sums of the path differences in section I and the rotated section I′ are canceled out ($\Delta L1 - \Delta L3 = 0$). The arc WG in

section III has the same length increment, with the bending radius having the same increment as S with the same open angle; thus, ΔL is determined only by section III. The path difference of section III can be also determined in a manner similar to that of section II. The construction details are provided in Ref. 10, with the only difference in our study being the removal of one arc WG in section I for a simplified layout and design calculation. Detailed descriptions of the calculation are also provided in Ref. 10.

The geometric parameters of section I, section I′, section II, and section III are shown in Figs. 4, 5(a), and 5(b).

Parameters $A1$ and $S2$ can be calculated with arbitrarily fixed initial parameters: W, H, $\Delta L1$, and S. The temporary total lengths of all the arrayed WGs were set from the initial parameters (WG$L1$ to WGLn). The target total lengths of the arrayed WGs were also set. Linear relationships were obtained by varying $S1$ of each WG in the proper range, i.e., WG$L1$ to WGLn versus $S1n$. Several iteration steps were performed for non-negative values of all parts. Simple equations for these calculations are described below.

The angle increment of the array is obtained from free-propagation-region geometric calculations. The angles of each WG in the array can be described as

$$Ain_n = Ain_1 - Del\_\delta \times (n-1), \tag{1}$$

where Del_δ represents the angle increment of the array from the focal point of the slab in radians and n the n'th array number. The height of each WG was set with the use of

$$H_n = H_1 - S \times (n-1), \tag{2}$$

where H represents the height and S spacing at the end of the arrayed WGs. The radius of the first arc can be described as

$$R1_n = \frac{H_n - S1_n \times \sin(Ain_n)}{1 - \cos(Ain_n)}, \tag{3}$$

where $R1$ denotes the radius of the first arc WG and $S1$ the length of the first straight WG, which is the subvariable parameter for optimization of the other lengths. The length of the first arc is

$$A1_n = R1_n \times Ain_n. \tag{4}$$

The length of the second straight WG is

$$S2_n = W - R_n \times \sin(Ain_n) - S1_n \times \cos(Ain_n), \tag{5}$$

where W denotes the width of section I or section I′, and the total length of each array from calculations for section I is

Table 2 Input and output taper geometry.

Taper geometry	Taper 1 (linear)		Taper 2 (exponential)		
	Width of taper (μm)	Length of taper (μm)	Width of taper (μm)	Length of taper (μm)	Exponential coefficient
Input	10	500	27	350	3
Output	13.5	1000	-	-	-
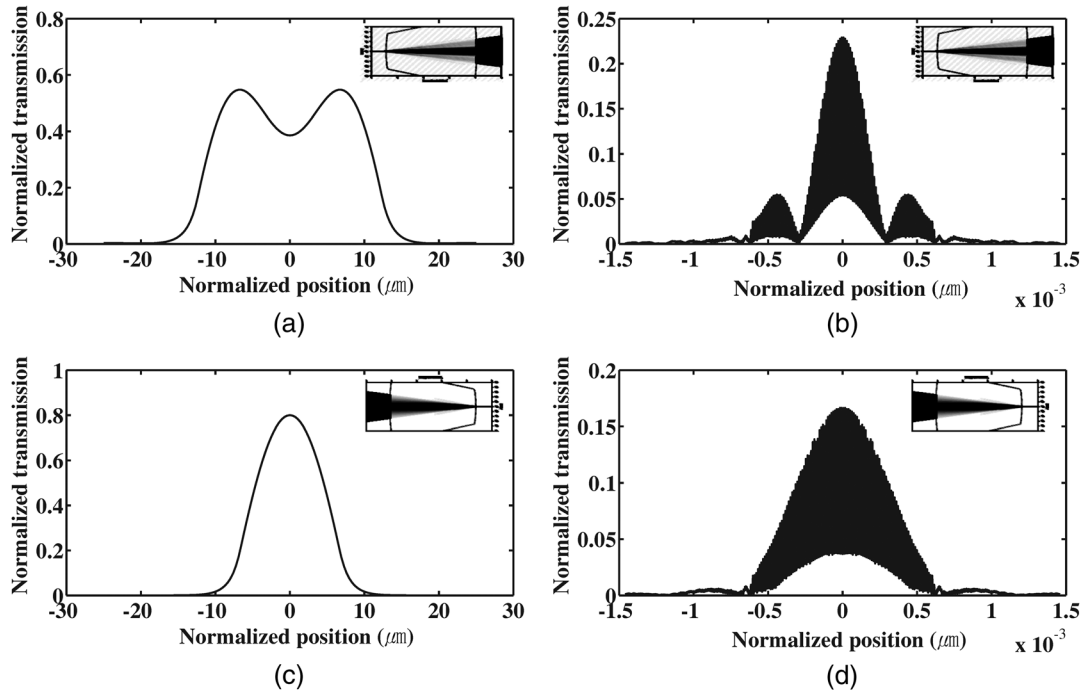
Fig. 1 Simulation results of (a) input taper mode shape, (b) far field of input slab, (c) output taper mode shape, and (d) far field of output slab.
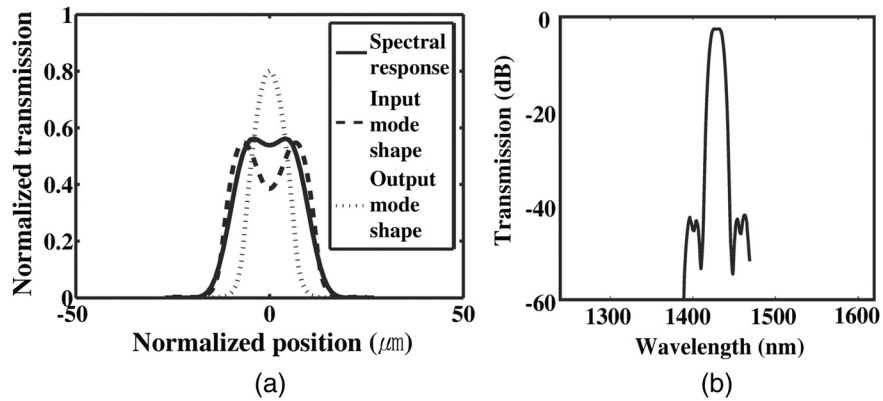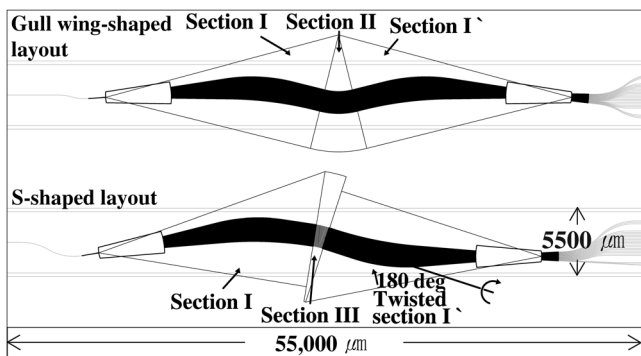

Fig. 2 (a) Simulation results of input and output coupled spectral shape and (b) center-to-center coupling simulation result.

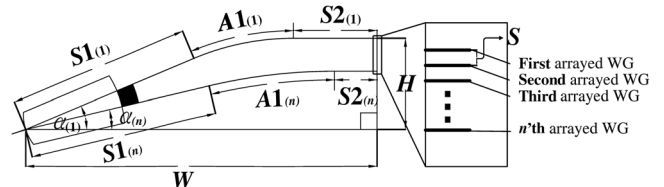$$WGL_n = S1_n + A1_n + S2_n. \tag{6}$$

To calculate the path difference relationship between the calculated total lengths of each array in section I, the reference array length is set with use of

$$RWGL_n = RWGL_1 - \Delta L \times (n-1). \tag{7}$$

Fig. 3 Schematic view of gull-wing-shaped layout and S-shaped layout.

Fig. 4 Geometry of section I (section I′) in AWG fabricated in the study.
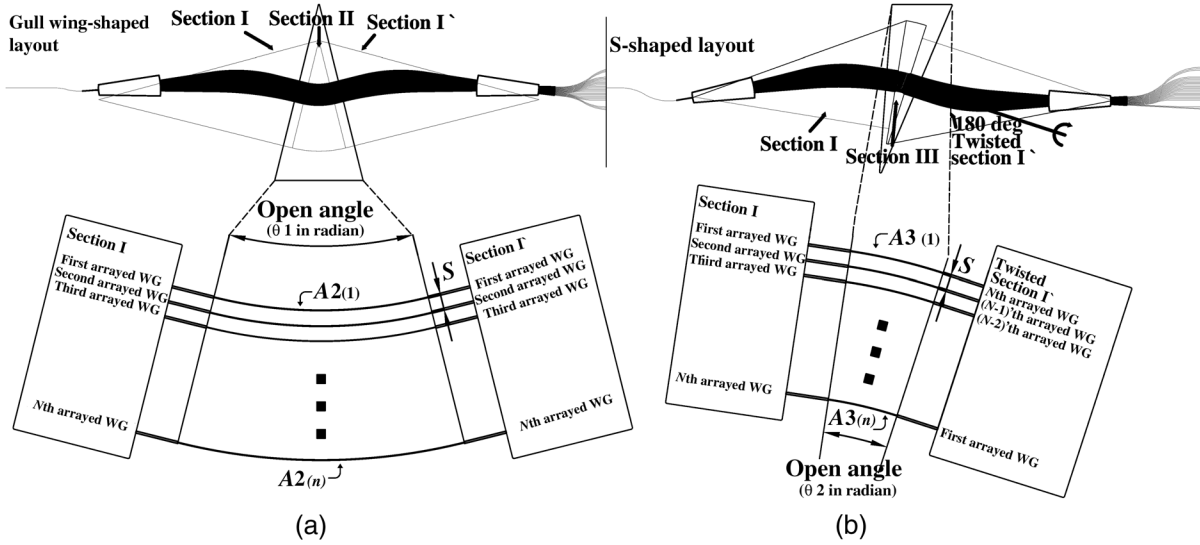
Fig. 5 Geometry of (a) section II and (b) section III in AWG fabricated in the study.
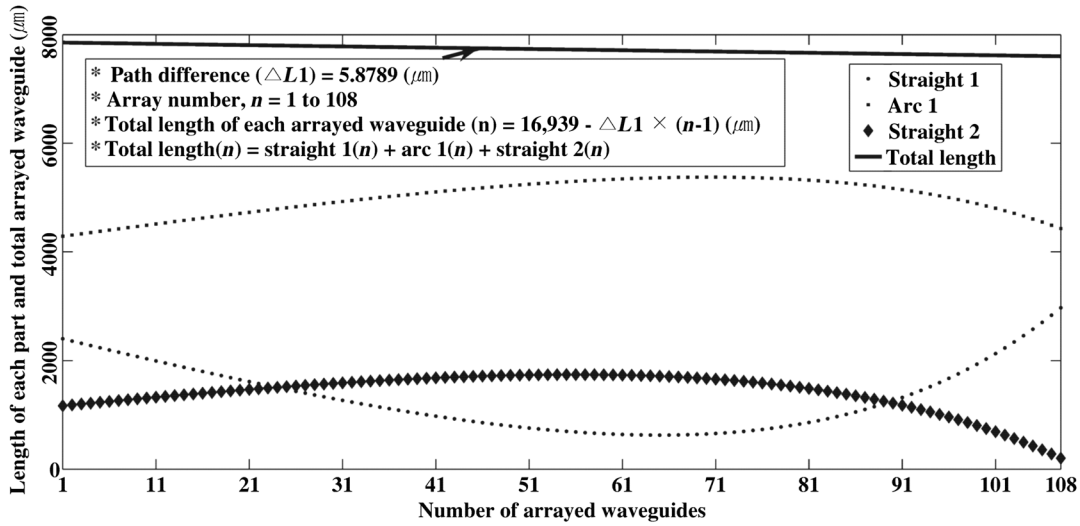

Fig. 6 Optimized layout values of section I (section I′).

The calculated total lengths of each array WG are calculated from the proper range of $S1n$. The difference between the end and start value is

$$\frac{\Delta WGL_n}{\Delta S1_n} = \frac{WGL_{n\_\mathrm{end}} - WGL_{n\_\mathrm{start}}}{S1_{n\_\mathrm{end}} - S1_{n\_\mathrm{start}}}. \qquad (8)$$

The optimized $S1n$ can be set with RWGLn from the slope and intercepts corresponding to Eq. (8). The optimized values of all components are shown in Fig. 6.

3 Fabrication and Measurement

We used a silica-on-silicon WG to fabricate our AWG. A 6-in.-silicon wafer (100) with 15-μm oxidization was used as the undercladding. The oxidized layer was formed by wet oxidation (Sungjin-Semitech SJF 2000) in a water–vapor atmosphere. A germanium-doped silica layer was deposited by plasma-enhanced chemical vapor deposition (Oxford Plasmalab System 100) and patterned by a lithography process with sputtered chromium (Sunic system in-line sputter)

and photoresist (AZ5214) to define the core pattern. A 150-nm-thick dc sputtered chromium film on the core layer was used as the hard mask material, and a 1.2-μm-thick photoresist was used to pattern the chromium layer. The chromium layer and the core layer were etched with an inductively coupled plasma etcher (Oxford Plasmalab 100) with the use of a Cl2/O2 mixture and C4F8/O2 mixture, respectively. The etch rate ratio of silica to chromium was greater than 31. The core layer was overetched down to 0.2 μm. A chromium etchant (Cyantek Cr-7SK) and buffered oxide etchant were used to eliminate the chromium layer and core sidewall residues. A phosphor and boron-doped overcladding layer was deposited by flame hydrolysis deposition after the wet cleaning process. Core layer consolidation and the overcladding layer reflow were achieved by means of the corresponding annealing processes.

The refractive index and diffusion depth of the undercladding layer were 1.45861 at 632.8 nm and 14.98 μm at the center point of the wafer, respectively. The core-undercladding index difference was ~1.02% at the center point of the
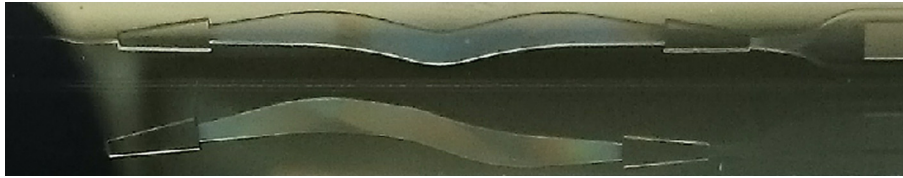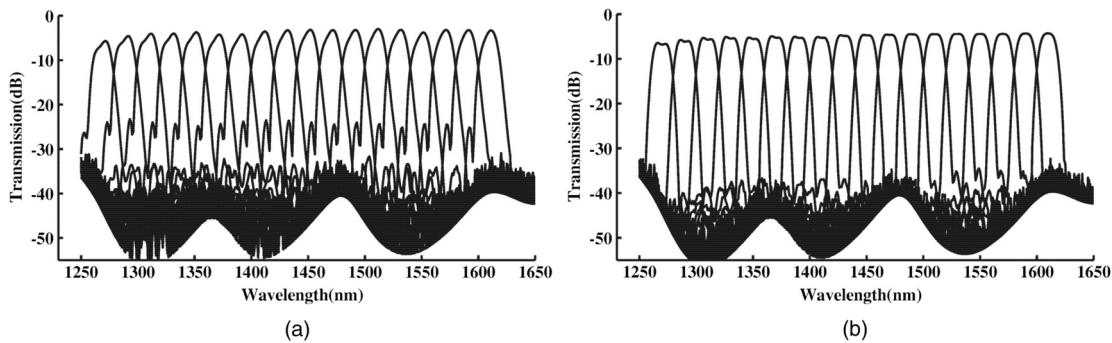
Fig. 7 Fabricated 18-channel CWDM AWG chip.

Fig. 8 Measurement results of (a) GW-shaped AWG and (b) S-shaped AWG.

wafer, and the thickness of the core layer was ∼6.01 μm. The deviation of the refractive index and core layer thickness over the wafer were less than 5%. The refractive index and the thickness of the overcladding layer at the center point of the wafer were 1.45854 at 632.8 nm and 15.18 μm, respectively. The properties of the undercladding layer and the overcladding layer were measured via ellipsometry (HORIBA-Jobin Yvon UVISEL ellipsometer). The properties of the core layer and the etch depth were monitored by a prism coupler (Sairontech SPA-4000) and an alphastep device (Tencor AS-200 Profilometer), respectively.

After chip dicing, (the chip is shown in Fig. 7) a broadband light source (Amonics ALS-CWDM Super-wideband light source), an optical spectrum analyzer (Agilent 81640B), and an automated translation stage with control driver (Suruga Seiki D250) were used for optical alignment and

Fig. 9 BER curves for back-to-back and after 10-km transmission with paired CWDM multiplexer and demultiplexer.

measurement. The vertical and horizontal alignment accuracies were less than 0.5 μm. The 2.5-Gbps bit error rate (BER) of the 18-channel CWDM AWG were measured by using directly modulated six CWDM distributed feedback laser diodes (1270, 1350, 1410, 1490, 1550, and 1610 nm) and calibrated photodiode with pseudorandom binary sequence 23 signals.

4 Results

The wavelength sweep was set to the range from 1250 to 1650 nm. The straight WG loss was ∼ − 1.6 dB. The spectra of the GW-shaped AWG in Fig. 8(a) exhibit distorted transmission because of stacked phase errors from the relatively long array path difference. However, the spectra from the S-shaped AWG in Fig. 8(b) are more favorable. It is assumed that the path difference tolerance is effectively reduced in the S-shaped layout because of path difference canceling. The insertion loss, 1-dB bandwidth, and adjacent crosstalk (13-nm bandwidth) of the S-shaped AWG in the worst-case scenario are −6.42 dB, 10.170 nm, and −19.5 dB, respectively. This result shows characteristics similar to those of commercial flat-top DWDM AWGs that use a silica-on-silicon WG.

The 2.5-Gbps BER measurement result of the S-shaped CWDM is shown in Fig. 9. As shown in Fig. 9, the sensitivity for back to back (B to B) was about −29 dBm. After 10-km transmission with two CWDM AWGs for multiplexing and demultiplexing, no significant transmission penalties were observed.

5 Discussion

In this study, we fabricated a flat-top wide-band 18-channel AWG with two layouts: GW and S-shaped layouts. The geometric parameters were calculated to understand a wide-band AWG with silica on silicone WGs. First, we observed the phase distortions from the initially fabricated GW-shaped AWG. The mismatching of the phase front from the output focal point was inferred from the observed slanted spectra. We examined the GW-shaped layout and calculated the
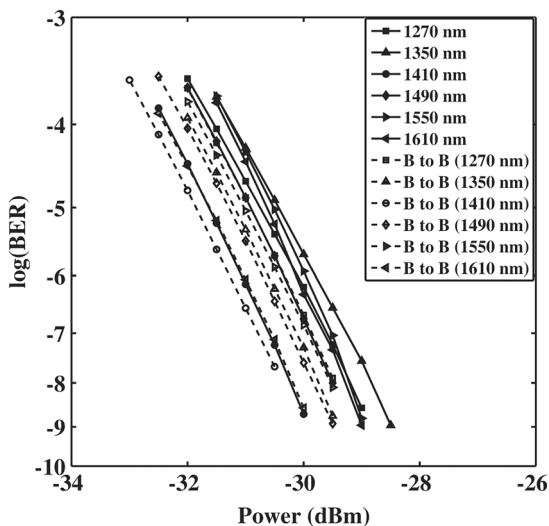
considerably high path differences in section I and section I′ over the total path difference to understand the AWG. Thus, we applied the S-shaped layout to minimize phase errors from the combination of section I and twisted section I′. The path difference to understand the AWG was only adjusted at the arc WGs between section I and twisted section I′; the S-shaped layout exhibited reduced phase error spectra with the path length difference canceling out in the CWDM wavelength range. The chip size for this layout is less than 5500 × 54,000 μm with 1.0 delta% refractive index contrast WG (40 AWGs can be arranged in a 6-in.-silicon wafer). Even though the fabricated AWG shows more insertion loss and adjacent crosstalk in comparison with thin film filters, it has the advantage of having a smaller footprint. Thus, it is suitable for use in subsidiary applications, such as portable power meters, because of its small size. In addition, our approach allows input/output design variations for communication multiplexers or demultiplexers that involve ultrawide Gaussian spectral shapes using input-output taper combinations or flat spectral shapes with single-mode input-multi-mode-output combinations.

6 Conclusion

In our study, we simulated and subsequently fabricated a wide-band 18-channel AWG with gull-wing-shaped and S-shaped layouts. Moreover, detailed calculations for the two layouts were performed to understand the AWG, and the previously reported layouts were experimentally verified with the AWG covering the full-channel CWDM grid. While the gull-wing-shaped layout did not provide the desired fidelity, the S-shaped layout yielded more favorable results in terms reduced phase error spectra. The performance of our AWG was comparable to that of commercial flat-top DWDM AWGs that use a silica-on-silicon WG. Our AWG offers the advantages of a small footprint and reduced cost, which makes it suitable for subsidiary applications such as optical power meters.

References

1. A. Banerjee et al., "Wavelength-division-multiplexed passive optical network (WDM-PON) technologies for broadband access: a review [Invited]," *J. Opt. Netw.* **4**(11), 737–758 (2005).
2. J. Pan et al., "Novel passive free space compact CWDM technology for outdoor applications," in *Optical Fiber Communication Conf. and Exposition and the National Fiber Optic Engineers Conference, Technical Digest (CD)*, Optical Society of America, (2006), paper NWD5.
3. H. Li et al., "Design of 1 × 8 silicon nanowire arrayed waveguide grating for on-chip arrayed waveguide grating demodulation integration microsystem," *Opt. Eng.* **51**(12), 123001 (2012).
4. H. Li et al, "Investigation of ultrasmall 1 × N AWG for SOI-based AWG demodulation integration microsystem," *IEEE Photon. J.* **7**(6), 7802707 (2015).
5. H. Li et al., "Practical fabrication and analysis of an optimized compact eight-channel silicon arrayed-waveguide grating," *Opt. Eng.* **52**(6), 064602 (2013).
6. C. Dragone, "An N × N optical multiplexer using a planar arrangement of two star couplers," *IEEE Photon. Technol. Lett.* **3**(9), 812–815 (1991).
7. M. K. Smit and C. Van Dam, "PHASAR-based WDM-devices: principles, design and applications," *IEEE J. Sel. Top. Quantum Electron.* **2**(2), 236–250 (1996).
8. K. Kodate and Y. Komai, "Compact spectroscopic sensor using an arrayed waveguide grating," *J. Opt. A. Pure Appl. Opt.* **10**(4), 044011–044018 (2008).
9. R. Adar et al., "Broad-band array multiplexers made with silica waveguides on silicon," *J. Lightwave Technol.* **11**(2), 212–219 (1993).
10. N. Ismail et al., "Improved arrayed-waveguide-grating layout avoiding systematic phase errors," *Opt. Express* **19**(9), 8781–8794 (2011).
11. I. Malitson, "Interspecimen comparison of the refractive index of fused silica," *J. Opt. Soc. Am.* **55**(10), 1205–1209 (1965).
12. M. K. Smit, "New focusing and dispersive planar component based on an optical phased array," *Electron. Lett.* **24**(7), 385–386 (1988).

Biographies for the authors are not available.